Steel and Composite Structures, *Vol. 56, No. 6 (2025) 499-512*
https://doi.org/10.12989/scs.2025.56.6.499

Classification of phases in alkali-activated glass powder using machine learning with Gaussian mixture model

Seunghoon Seo[1], Yujin Lee[2], Young K. Ju[1], Ilhwan You*[3] and Goangseup Zi[1]

[1]*School of Civil, Environmental and Architectural Engineering, Korea University, 145 Anam-ro, Seongbuk-gu, Seoul, 02841, Republic of Korea*
[2]*Department of Structural Engineering Research, Korea Institute of Civil Engineering and Building Technology, 283, Goyangdae-Ro, Ilsanseo-Gu, Goyang-Si, Gyeonggi-Do, 10223, Republic of Korea*
[3]*Department of Rural Construction Engineering, Jeonbuk National University, 567 Baekje-daero, Deokjin-gu, Jeonju-si, 54896, Jeollabuk-do, Republic of Korea*

(Received July 14, 2025, Revised August 15, 2025, Accepted August 25, 2025)

Abstract. Traditional methods for classifying micromechanical properties in alkali-activated materials depend on manual correlation of nanoindentation data, which is both time-consuming and subjective. This study examines the application of unsupervised machine learning to automate phase identification in alkali-activated glass powder and blast furnace slag. Grid nanoindentation was combined with scanning electron microscopy and energy dispersive X-ray spectroscopy to uncover heterogeneous phase assemblages. A Gaussian mixture model (GMM) was utilized to distinguish among the outer matrices, particles, rims, and their respective proportions. The GMM-based results were compared with those obtained through manual classification. The optimal number of clusters was determined using the Bayesian information criterion. Accuracy was assessed based on phase prediction error and normalized center prediction error. The tied covariance model with eight clusters showed the highest agreement with manually classified phases, which minimizes centroid and phase fraction errors. This approach enables robust, quantitative evaluation of micromechanical properties in glass-based phases, significantly reducing the need for manual classification.

Keywords: alkali-activated material; Gaussian mixture model; glass powder; machine learning; nanoindentation

1. Introduction

Soda-lime glass, an amorphous silicate material, is one of the most widely consumed industrial products due to its affordability, thermal resistance, and transparency (Lu *et al.* 2017). However, its widespread use results in the generation of over 1.3 million tons of waste glass annually; a significant portion of this waste is soda-lime glass, but only a fraction is currently recycled (Ferdous *et al.* 2021, Jani and Hogland 2014, Shi and Zheng 2007, Yoo *et al.* 2022b, You *et al.* 2021, 2023b). To promote recycling and mitigate environmental impact, waste glass is often processed into fine glass powder (GP). GP can act pozzolanically or participate in alkaline activation, and has been explored as a supplementary cementitious material in cement composites (Adesina and Das 2020, Canakci *et al.* 2016, Du and Tan 2017, Idir *et al.* 2011, Kalakada *et al.* 2020, Mirzahosseini and Riding 2015, Samarakoon *et al.* 2020, Shayan and Xu 2006, Shi *et al.* 2005, Yoo *et al.* 2022b, You *et al.* 2021, 2023b).

Recently, GP has also been utilized as a precursor for alkali-activated materials (AAMs) thanks to its potential to create cement-free binders (He *et al.* 2020, Lu and Poon 2018, Samarakoon *et al.* 2020, Sun *et al.* 2021a, Xiao *et al.* 2021, You *et al.* 2022, 2023b). However, excessive use of GP introduces several challenges. Its high silica and sodium content can lead to alkali–silica reaction, while its low-calcium and aluminum limits polymerization and gel formation. These factors can result in poor mechanical strength and dimensional instability (He *et al.* 2020, Rajabipour *et al.* 2015, Saccani and Bignozzi 2010, Zhang *et al.* 2020). In addition, elevated alkalinity may cause alkali leaching, and the absence of reactive calcium suppresses the formation of C–A–S–H gels (Lu and Poon 2018, Xiao *et al.* 2021, Zhang and Zhai 2021).

To address these limitations, several studies have proposed the combined use of GP and calcium-rich precursors such as blast-furnace slag (BFS) (Maraghechi *et al.* 2017, Mota Gassó 2015). BFS is abundant in calcium and aluminum, which facilitates the formation of cross-linked C–(N)–A–S–H gel. In this context, GP provides silica and sodium, which are essential for supporting polymerization and maintaining pH stability. Cercel *et al.* (2021) showed that GP–BFS blends activated with alkali solutions could achieve compressive strengths comparable to those of Portland cement. Maraghechi *et al.* (2017) also reported enhanced reactivity and polymerization in GP–BFS systems, with sodium ions from GP promoting further condensation. These findings suggest that incorporating BFS can alleviate the limitations of GP, which enhances material stability through complementary chemical contributions.

*Corresponding author, Ph.D. Professor
E-mail: ih-you@jbnu.ac.kr

ISSN: 1229-9367 (Print), 1598-6233 (Online)

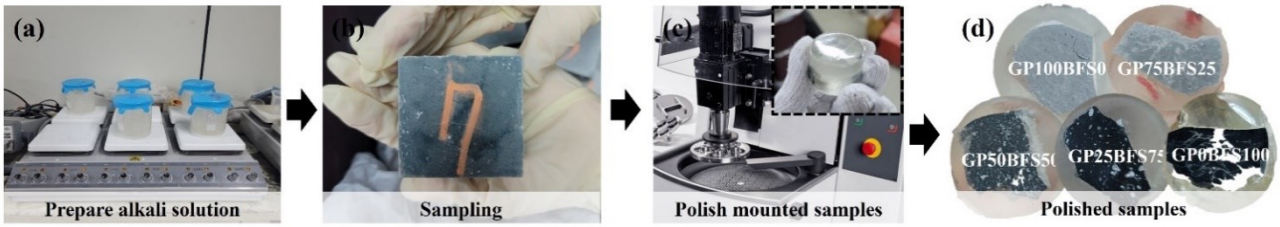

Fig. 1 Procedure for sample preparation

Despite recent advancements, many studies primarily concentrated on the bulk mechanical behavior of alkali-activated binders, often neglecting the micromechanical behavior of the individual phases within GP–BFS systems. These binders are inherently heterogeneous, consisting of unreacted particles, partially dissolved rims, and multi-phase gel matrices. The interactions among these elements, spanning from nano- to microscales, significantly influence the macromechanical behavior. Recent research highlights a strong correlation between macroscopic mechanical properties and the micromechanical characteristics of the constituent phases (Fang and Zhang 2020, Hu and Li 2015).

In response to this need, multimodal approaches have been developed, integrating nanoindentation with microstructural imaging techniques. Hu and Li (2014) showed that coupling nanoindentation with scanning electron microscopy (SEM)-based phase segmentation allows for the identification of distinct phases such as Portlandite, clinker residue, and C–S–H gel in cement pastes. Wilson *et al.* (2017, 2019) and Jia *et al.* (2020) further employed nanoindentation–energy dispersive spectroscopy (EDS) mapping to classify micromechanical clusters in natural pozzolan and GP systems, illustrating how partially reactive inclusions and gel heterogeneity affect phase distribution. However, these methods typically rely on manual matching between indentation locations and image-based phase maps, a labor-intensive process that is susceptible to subjectivity.

Statistical approaches such as histogram deconvolution have been used to estimate phase properties from indentation data (Hu and Li 2014, Nemecek *et al.* 2011). These approaches that the micromechanical properties obtained from a set of nanoindentation measurements represent the deconvolution of the distribution of different phases, including unreacted particles, interfacial rims (hereafter referred to as “rim”), and outer matrices (hereafter referred to as “outer”). The micromechanical properties of the individual phases are extracted through a statistical deconvolution of these measurements.

Although this approach is well-supported by Chen *et al.* (2021), Luo *et al.* (2021). Exploring different sets of statistical models for individual phases during the analysis is essential. Given the large number of samples generated from nanoindentation operations developing an automated method for rapid statistical deconvolution is highly recommended.

Unsupervised machine learning has been introduced to classify indentation data without prior phase labeling. Among various precursors, alkali-activated fly ash (FA) has been widely studied as an effective precursor in the field of AAMs. Notably, Luo *et al.* (2021, 2020a) employed Gaussian mixture models (GMMs) with maximum likelihood estimation (MLE) to more robustly identify overlapping phase distributions in FA-based systems. Chen *et al.* (2021) compared GMM with a deterministic clustering method, K-medoids, using nanoindentation datasets. Although K-medoids exhibited greater stability with limited data, it requires predefined cluster numbers and user-defined initial centers, which diminish the objectivity and reproducibility of the results. This limitation is especially critical for systems with overlapping or transitional phases.

By contrast, GMM assigns data points to phases based on probabilities rather than fixed thresholds. This allows for a more realistic representation of the continuous transitions in micromechanical properties between phases. For this reason, GMM was adopted in this study to enable a more reliable capture of the heterogeneity of AAMs. Arachchige *et al.* (2024) applied this approach to 11 AAMs. They showed a strong correlation between nanoindentation cluster data and reaction products. These studies illustrate that micromechanical heterogeneity can be analyzed effectively using unsupervised machine learnings. However, most of these applications have focused on fly ash-based binders, leaving the analysis of GP–BFS systems unexplored.

Few studies have investigated AAMs based on GP, despite growing interest in its use as a low-calcium, silica-rich precursor. In contrast to FA, GP is characterized by limited intrinsic reactivity due to its low calcium and aluminum content and high silica-to-alumina ratio, often resulting in weakly polymerized sodium-rich gels (Ali *et al.* 2023, Gao *et al.* 2020, Lu and Poon 2018, Lu *et al.* 2017). This composition leads to prolonged setting times, lower early strength, and poorer interfacial zones compared to FA or slag-based systems. These differences suggest that the phase characteristics of GP-based AAMs may differ significantly from those of FA-based AAMs. However, no prior study has applied the unsupervised clustering technique to classify mechanical phases in GP–BFS composites using nanoindentation data nor validated the classifications through microstructural analysis.

In this study, the GMM clustering technique was employed to analyze grid nanoindentation data from two single-precursor alkali-activated composites (GP- and BFS-only) as well as a binary composite (GP and BFS). The phase-level interpretation was enhanced through microstructural analysis conducted in conjunction with

Table 1 Chemical and physical characteristics of used precursors

Content [%]	SiO_2	Al_2O_3	Fe_2O_3	CaO	MgO	SO_3	Na_2O	K_2O	Others	D_{50} [μm]	Crystallinity [%]
GP	69.4	2.1	0.6	10.5	1.8	0.1	14.0	0.8	0.7	12.7	1.5
BFS	31.6	13.0	0.5	46.3	3.0	3.8	0.3	0.5	1.1	13.1	43.8

Table 2 Mix proportions of alkali-activated materials, where W/P = 0.35

Mixture ID	Solution [kg/m^3]			Binder [kg/m^3]		Precursor to water molar ratio	
	Water	SS	SH	GP	BFS	GP	BFS
GP100BFS0	524	252	84	1,498	0	2.86	-
GP75BFS25				1,124	375	2.15	0.71
GP50BFS50				749	749	1.43	1.43
GP25BFS75				375	1,124	0.71	2.15
GP0BFS100				0	1,498	-	2.86

SEM–backscattered electron (BSE) imaging and EDS chemical mapping. Utilizing the integrated dataset, we identified distinct phases and quantitatively evaluated the heterogeneity of the composites. The results indicate that GMM offers a scalable framework for classifying micromechanical properties in chemically complex AAMs.

The remainder of this paper is organized as follows. Section 2 outlines the experimental procedures, which include nanoindentation and microstructural characterization, as well as data analysis methods that utilize unsupervised machine learning and evaluation techniques for results. Section 3 presents the results and discusses the experiments and provides an interpretation of GMM. Section 4 concludes the study.

2. Experimental and data analysis methods

2.1 Raw materials

Table 1 presents the chemical compositions and physical properties of GP and BFS. BFS exhibited a fineness of 3,564 cm^2/g and was sourced from a commercial supplementary cementitious material producer. GP was produced by grinding waste soda-lime cullet obtained from a local disposal company, with its particle size distribution adjusted to align with that of BFS to minimize differences in reactivity due to fineness. The D_{50} values for GP and BFS were 12.7 μm and 13.1 μm, respectively. X-ray diffraction analysis indicated that GP had a crystallinity of 1.5%, confirming its predominantly amorphous phase, whereas BFS exhibited 43.8% crystallinity (You *et al.* 2023a). BFS contained higher levels of CaO (46.3%) and Al_2O_3 (13.0%) than GP, which was rich in SiO_2 (69.4%) and Na_2O (14.0%).

2.2 Sample preparation

Table 2 summarizes the mix proportions. The water-to-precursor ratio (W/P), molarity of sodium hydroxide (SH), and sodium silicate-to-sodium hydroxide ratio (SS/SH) were set to 0.35, 4, and 3, respectively, considering suitable rheological properties and compressive strength of AAMs (Yoo *et al.* 2022a, You *et al.* 2023a). Five mixture types were prepared: GP100BFS0 (100% GP), GP75BFS25, GP50BFS50, GP25BFS75, and GP0BFS100 (100% BFS), enabling a comprehensive investigation into micromechanical heterogeneity across different precursor combinations.

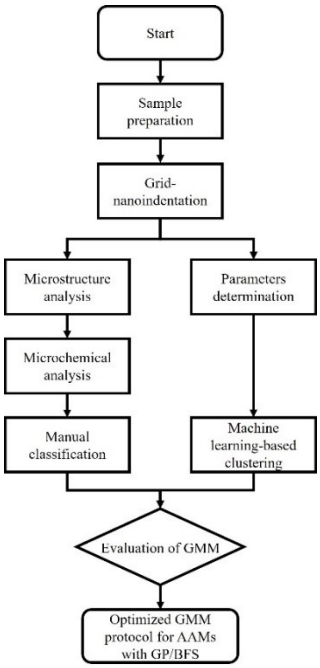

Fig. 2 Workflow for phase classification using grid-nanoindentation and GMM

The powder components were dry-mixed for 30 seconds using a laboratory mixer. The alkali activator was prepared by combining SS and SH with deionized water. SS was utilized in powder form (extra pure grade), whereas SH was provided as 98% pure beads. Prior to being mixed with the precursor, the solution was magnetically stirred and allowed to cool at room temperature for 1 day. A polycarboxylate-based superplasticizer (0.2 wt.% of binder) was added to the

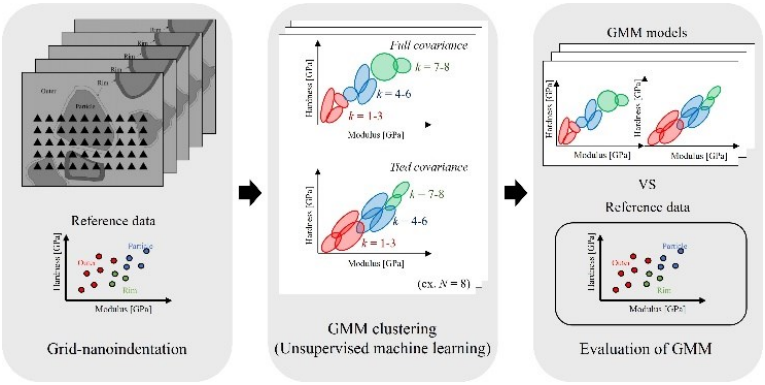

Fig. 3 Schematic workflow for micromechanical phase classification in AAMs using GMM

alkali solution to enhance the dispersion and workability of the precursor powders. After an additional 2 minutes of mixing, the fresh paste was cast into cube molds that had

been coated with a release agent. All specimens were demolded 1 day after casting, then cured in water at 20°C for 6 days, followed by thermal curing at 85°C for 1 day to promote geopolymerization (Singh *et al.* 2015). However, GP100BFS0 and GP75BFS25 mixtures exhibited significantly delayed setting behavior, requiring 6 days before demolding. This delay could be attributed to the low alkali reactivity of GP, derived from its limited calcium and aluminum content, which in turn suppressed early polymerization (He *et al.* 2020).

Fig. 1 illustrates the sequence of specimen preparation. To minimize wall effect and surface irregularities, cylindrical cores were extracted using a concrete cutter. These cores were embedded in fast-curing epoxy resin and left to cure for 1 day. Each mounted specimen was polished using a series of abrasive papers of grades #400, #800, #1,200 and #2,000 for 30 minutes sequentially. This ensured a flat and uniform surface essential for reliable grid nanoindentation.

2.3 Methods for manual classification

Fig. 2 illustrates the experimental procedure. To ensure consistent indentation depth and minimize surface irregularities, the surface roughness of polished specimens was measured using atomic force microscopy in non-contact mode. Based on these measurements, the indentation depth for nanoindentation was fixed at 400 nm. A 5 × 10 indentation grid was defined on each sample. A spacing of 10 μm was used based on the particle size and rim width, allowing multiple indentations within interfacial regions without overlapping adjacent features.

Nanoindentation was performed under a maximum load of 2 mN, followed by 5 seconds holding time at peak load to stabilize the response. The maximum load (2 mN) and holding time (5 seconds) were necessary to maintain a penetration depth of 400 nm and to ensure stable unloading, respectively. Outliers were removed based on physical reasoning. Indentation points with extremely low modulus or hardness (near zero), likely due to pores or debris, and data points far outside the main *E–H* scatter were excluded prior to clustering. These parameters were determined based on experimental requirements, as no standardized specifications exist for nanoindentation of AAMs. See Appendix A for details on the grid nanoindentation procedure.

Upon alkali activation, the precursor particles were partially dissolved, leading to the formation of a reaction front known as the "rim." For clarity, rims surrounding GP particles and BFS particles are hereafter referred to as "G-rim" and "B-rim," respectively. The activation progressed outward into a more homogeneous gel matrix, referred to as the outer product. This resulted in three zones: unreacted particles (hereafter referred to as GP particle or BFS particle based on its precursor), rims, and outers. These were visualized using BSE imaging in grayscale, and their compositions analyzed through EDS mapping and line scanning. SEM–EDS analyses were performed on the same areas previously subjected to nanoindentation, ensuring consistency between micromechanical measurements and microstructural observations. Nanoindentation data were categorized accordingly and used as a reference for evaluating the probabilistic classification generated by machine learning.

2.4 Machine learning-based data analysis

Machine learning algorithms are typically classified into supervised and unsupervised approaches. Supervised learning predicts output variables based on labeled input data. For instance, artificial neural networks have been used to predict durability parameters such as calcium leaching depth based on multiple input conditions (Lee *et al.* 2023). These approaches are effective when extensive labeled data are available for training.

In this study, the aim is to classify phases from unlabeled nanoindentation data, using only the indentation modulus and hardness as input features. Since the phase identity of each nanoindentation point is unknown, GMM was employed to infer the latent phase clusters from the measured data (Fig. 3). The performance of this unsupervised classification is later evaluated by comparison to manually labeled phases based on microstructural locations identified through SEM–EDS imaging.

GMM assumes each data point $x_i \in R^M$ is generated from a weighted sum of N multivariate normal distributions. The probability density function is given by

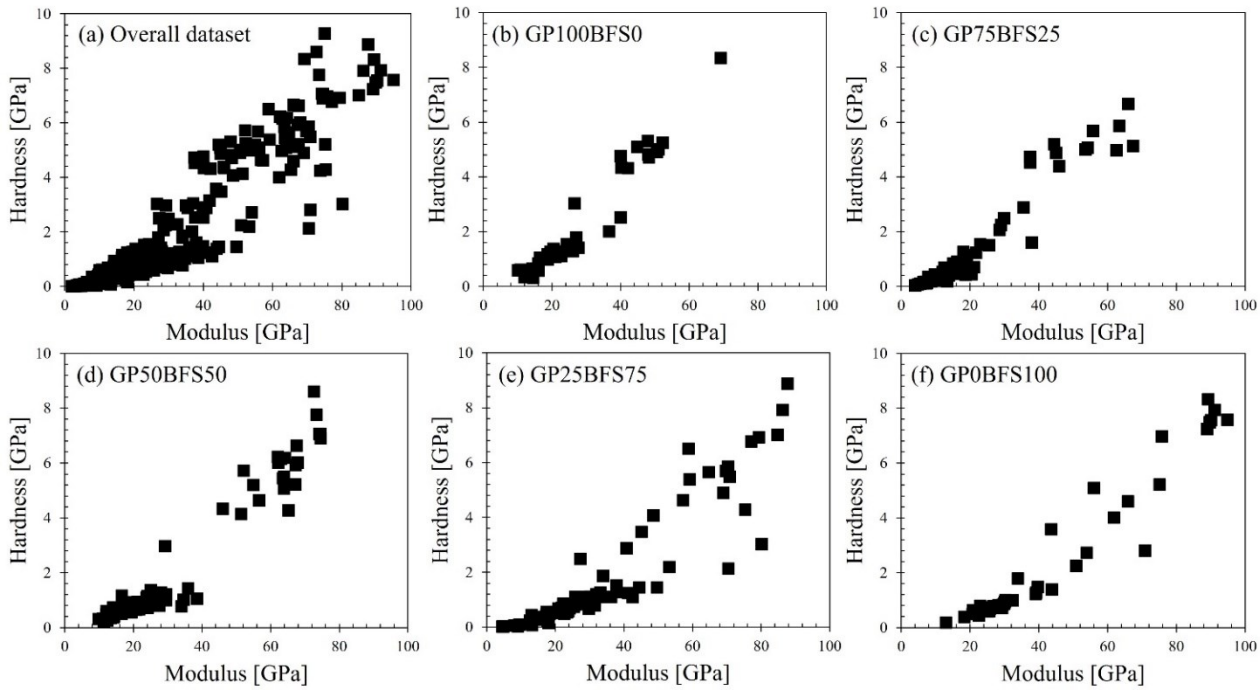

Fig. 4 Unlabeled elastic modulus and hardness distributions obtained from grid-nanoindentation

$$f(x) = \sum_{k=1}^{N} w_k \, \mathcal{N}(x \mid \mu_k, C_k) \tag{1}$$

where w_k is the mixing coefficient, μ_k is the mean vector, and C_k is the covariance matrix of the k-th Gaussian component, respectively. The function $\mathcal{N}(x|\mu_k, C_k)$ denotes the multivariate normal distribution with mean μ_k and covariance C_k, and the mixing coefficients satisfy $\sum_{k=1}^{N} w_k = 1$.

These parameters are estimated using the MLE framework, which is implemented through the expectation-maximization (EM) algorithm. The EM algorithm iteratively calculates the posterior probability that each data point belongs to each Gaussian component, and then updates the model parameters based on these probabilities. This iterative process increases the overall likelihood with each cycle. Every data point is probabilistically associated with all components with the component exhibiting the highest probability typically regarded as the dominant cluster. The log-likelihood function is given by

$$\log L = \sum_{i=1}^{N_d} \log f(x_i) \tag{2}$$

where $f(x_i)$ is the marginal probability of data point x_i, and N_d is the total number of observed data.

GMMs can approximate any probability distribution, and models with more components often achieve better fit. To penalize excessive model complexity, the Bayesian information criterion (BIC) was selected as it imposes a stronger penalty than the Akaike information criterion, which tends to favor models with a greater number of components due to its weaker complexity penalty (Bishop and Nasrabadi 2006, Luo *et al.* 2020a, Schwarz 1978). BIC is given by

$$\mathrm{BIC} = -2 \log L + p \log N_d \tag{3}$$

where log L is the maximum log-likelihood, p is the number of estimated parameters, and N_d is the number of data points. Models with lower BIC values than others were chosen as the optimal model candidates.

2.5 Evaluation metrics for clustering performance

Two quantitative error metrics were introduced to evaluate how effectively a given GMM configuration reproduces the manually identified phase structure. The centroid error of the k-th cluster d_k is given by

$$d_k = \sqrt{\left(\frac{E_k^{\mathrm{pre}} - E_k^{\mathrm{exp}}}{\sigma_E}\right)^2 + \left(\frac{H_k^{\mathrm{pre}} - H_k^{\mathrm{exp}}}{\sigma_H}\right)^2} \tag{4}$$

where E_k^{pre} and H_k^{pre} are the predicted elastic modulus and hardness of cluster k, and E_k^{exp} and H_k^{exp} are the corresponding manual centroids, respectively. The terms σ_E and σ_H denote the global standard deviations of modulus and hardness, respectively, and are used to normalize the differences between predicted and reference values. The average centroid error D_N is given by

$$D_N = \frac{1}{N} \sum_{k=1}^{N} d_k \tag{5}$$

where N is the total number of clusters.

The total phase-fraction error δ_N is given by

$$\delta_N = \sum_{k=1}^{N} \left| w_k^{\mathrm{pre}} - w_k^{\mathrm{exp}} \right| \tag{6}$$

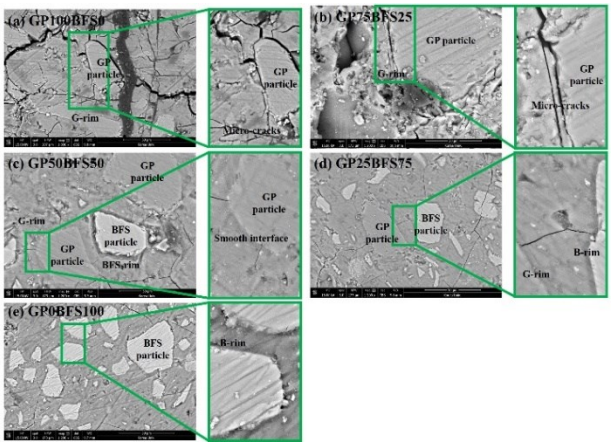

Fig. 5 Microstructures observed by BSE imaging

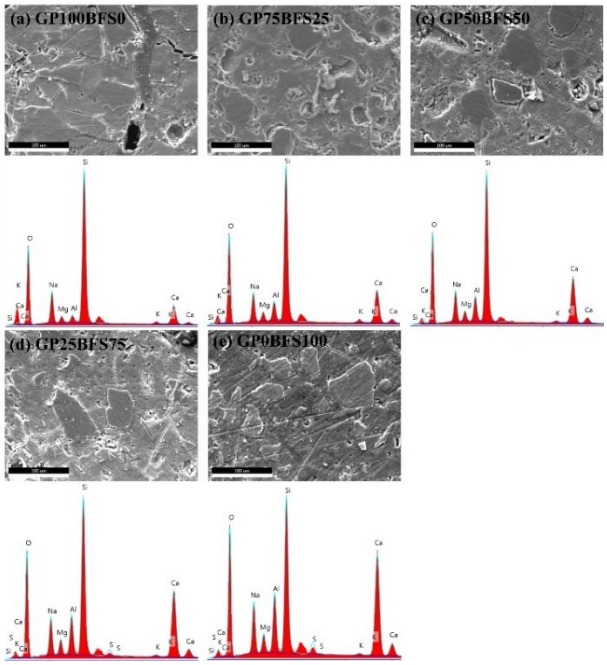

Fig. 6 SEM images and corresponding EDS spectra of AAMs under varying GP/BFS ratios

where w_k^{pre} and w_k^{exp} are the predicted and experimental volume fractions of phase k, respectively. Both D_N and δ_N reach zero when the predicted clusters perfectly match the manual reference. Therefore, lower values indicate better clustering performance.

3. Results and discussion

3.1 Manual classification

3.1.1 Unlabeled micromechanical properties

Fig. 4 shows raw E–H scatter plots obtained from 250 indents for each mixture. All mixtures exhibit a dense cluster at E < 20 GPa and H < 1 GPa, corresponding to weak, porous gels formed in low-calcium AAMs (Arachchige *et al.* 2024, Luo *et al.* 2020a). As the BFS content increases the data cloud shifts toward higher modulus and hardness values. The BFS-rich mixtures GP25BFS75 and GP0BFS100, exhibit a clear separation between low-stiffness gels and high-stiffness components such as dense Ca-rich products or unreacted BFS particles.

This observed range aligns with earlier nanoindentation studies, which reported 10–20 GPa for low-Ca gels and values greater than 50 GPa for dense or unreacted phases (Königsberger *et al.* 2022, Sun *et al.* 2021b).

3.1.2 Microstructural observations of reaction phases

The morphological characteristics of AAMs were analyzed using BSE imaging, as shown in Fig. 5. The micrographs were utilized to evaluate rim formation and the distribution of microcracks. In GP100BFS0 and GP75BFS25 (Figs. 5(a) and 5(b)), the grayscale levels appeared relatively uniform, where minimal contrast was observed between the GP particles and surrounding matrix. Rims were faintly visible but not clearly defined, and visible microcracks often appeared along particle boundaries and within the matrix. This suggests limited reaction at the particle–matrix interface and poor morphological separation.

These characteristics were more pronounced in GP100BFS0, possibly due to restricted gel formation in the absence of BFS. The poorly developed rims and the limited formation of reaction zones in GP100BFS0 are consistent with previous studies, which indicated that in the absence of reactive calcium sources, alkali-activated glass powder primarily forms sodium silicate hydrate (N–S–H) gels characterized by low connectivity and amorphous structure (Rajabipour *et al.* 2015, You *et al.* 2023a). These gels are often weakly cross-linked and mechanically fragile, leading to microcracking and unstable interfaces in the hardened matrix.

In the GP50BFS50 sample (Fig. 5(c)), the contrast between particles and the surrounding gel increased, and the rims became more distinguishable. Microcracks were less frequent, and the matrix appeared denser compared to GP-rich materials. In GP25BFS75 and GP0BFS100 (Figs. 5(d) and 5(e)), distinct rims surrounding BFS particles were observed that featured smoother and more continuous particle–matrix interfaces with minimal visible cracks. These features can be attributed to a greater extent of reaction and increased gel formation, likely due to the Ca- and Al-rich composition of BFS.

3.1.3 Chemical composition and phase development

The chemical composition of AAMs was analyzed using SEM images and the corresponding EDS spectra, as depicted in Fig. 6. The EDS spectra represent averaged compositions across the full range of SEM image areas. In the GP100BFS0 sample, high intensities of Si and Na were observed, whereas Ca and Al were nearly absent. This chemical profile suggests limited calcium-based reactions, consistent with the formation of N–S–H gels in low Ca systems (Rajabipour *et al.* 2015, Zhang *et al.* 2020). Rim structures were not clearly defined in the BSE image.

As the BFS content increased, the peaks for Ca and Al became significantly stronger. In GP75BFS25 and GP50BFS50, observed areas were rich in Ca and Al, which may be attributable to BFS. In the BFS-dominant mixtures

Table 3 Mean and standard deviations of elastic modulus and hardness derived from manual phase classification

Mixture ID	Property	μ ± σ [GPa]				
		Outer	GP	G-rim	BFS	B-rim
GP100BFS0	*E*	21.4 ± 7.5	46.7 ± 9.5	17.6 ± 11.8	-	-
	H	1.2 ± 0.6	5.0 ± 1.2	0.8 ± 0.8	-	-
GP75BFS25	*E*	13.3 ± 6.6	49.2 ± 15.4	15.3 ± 6.1	40.2 ± 7.4	19.8 ± 7.2
	H	0.6 ± 0.5	4.7 ± 1.6	0.3 ± 0.1	3.9 ± 1.0	1.2 ± 0.8
GP50BFS50	*E*	17.9 ± 5.0	57.3 ± 11.8	28.6 ± 4.7	64.9 ± 10.1	36.8 ± 18.7
	H	0.7 ± 0.2	5.6 ± 1.4	1.2 ± 0.2	5.6 ± 1.8	2.3 ± 2.2
GP25BFS75	*E*	22.1 ± 7.6	40.1 ± 6.0	28.2 ± 5.3	59.0 ± 20.6	43.3 ± 6.0
	H	0.7 ± 0.3	2.4 ± 2.6	1.2 ± 0.7	4.2 ± 2.4	2.1 ± 1.2
GP0BFS100	*E*	26.9 ± 10.2	-	-	61.9 ± 25.0	40.4 ± 21.0
	H	0.8 ± 0.5	-	-	4.6 ± 2.7	1.9 ± 2.2

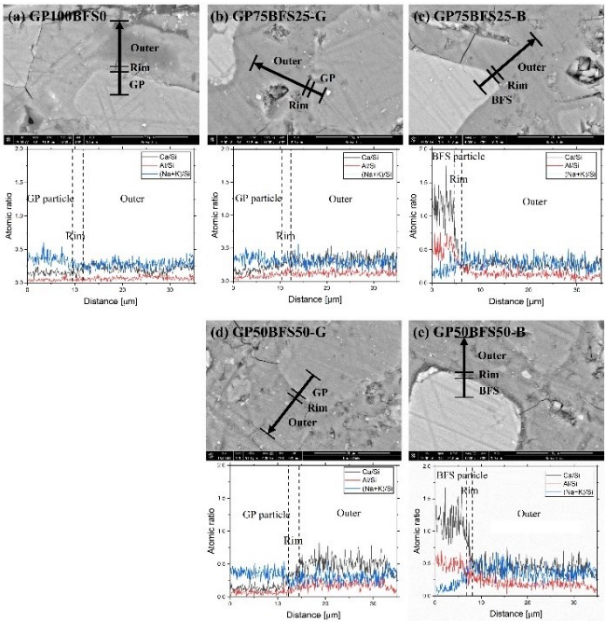

Fig. 7 Scanned line on BSE images and results of EDS line scanning

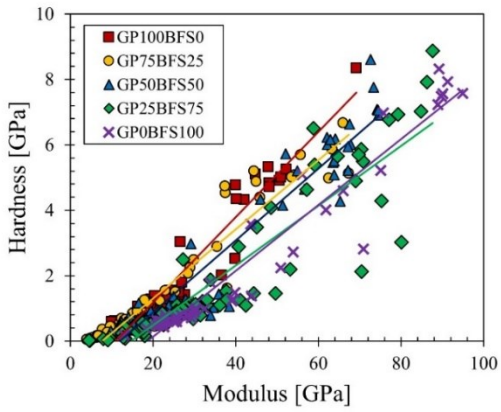

Fig. 8 Hardness–modulus scatter plots for each mixture

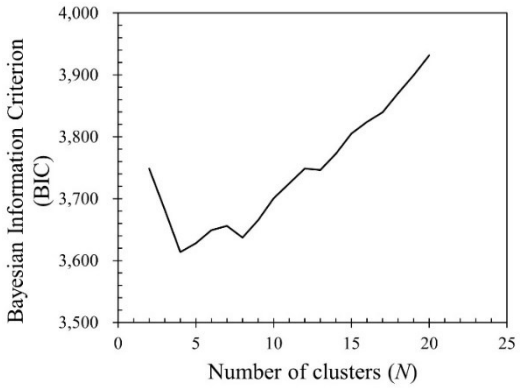

Fig. 9 Bayesian Information Criterion (BIC) plotted as a function of the number of clusters (*N*) for Gaussian mixture models

(GP25BFS75 and GP0BFS100), well-defined rims and strong signals for Ca and Al signals were observed around the particles and throughout the matrix. These results confirm that increasing BFS content includes rim formation and more distinct phase development.

The line scanning results shown in Fig. 7 illustrate chemical transitions across unreacted particles, rim regions, and the outer. In GP100BFS0 and GP75BFS25-G (Figs. 7(a) and 7(b)), where GP is the dominant precursor, the Ca/Si and Al/Si ratios remained steady along the scanned lines, indicating minimal chemical contrast between the unreacted particle and the outer. A slight change in (Na+K)/Si and Ca/Si ratios at the particle boundary suggests the presence of a weakly-developed G-rim.

By contrast, GP75BFS25-B and GP50BFS50-B (Figs. 7(c) and 7(e)) show clear Ca and Al peaks near the BFS particles, indicating the formation of B-rims. GP50BFS50-G (Fig. 7(d)) also exhibited noticeable variation in chemical ratios across the GP–rim–outer interface, with G-rim thickness estimated to be less than 5 μm. These results confirm that gradual chemical gradients and rim development occur primarily in BFS-containing mixtures.

3.1.4 Micromechanical properties analysis by manual classification

Manual classification of indentation points was conducted based on SEM imaging. Each indent's location was visually identified in BSE images to determine whether

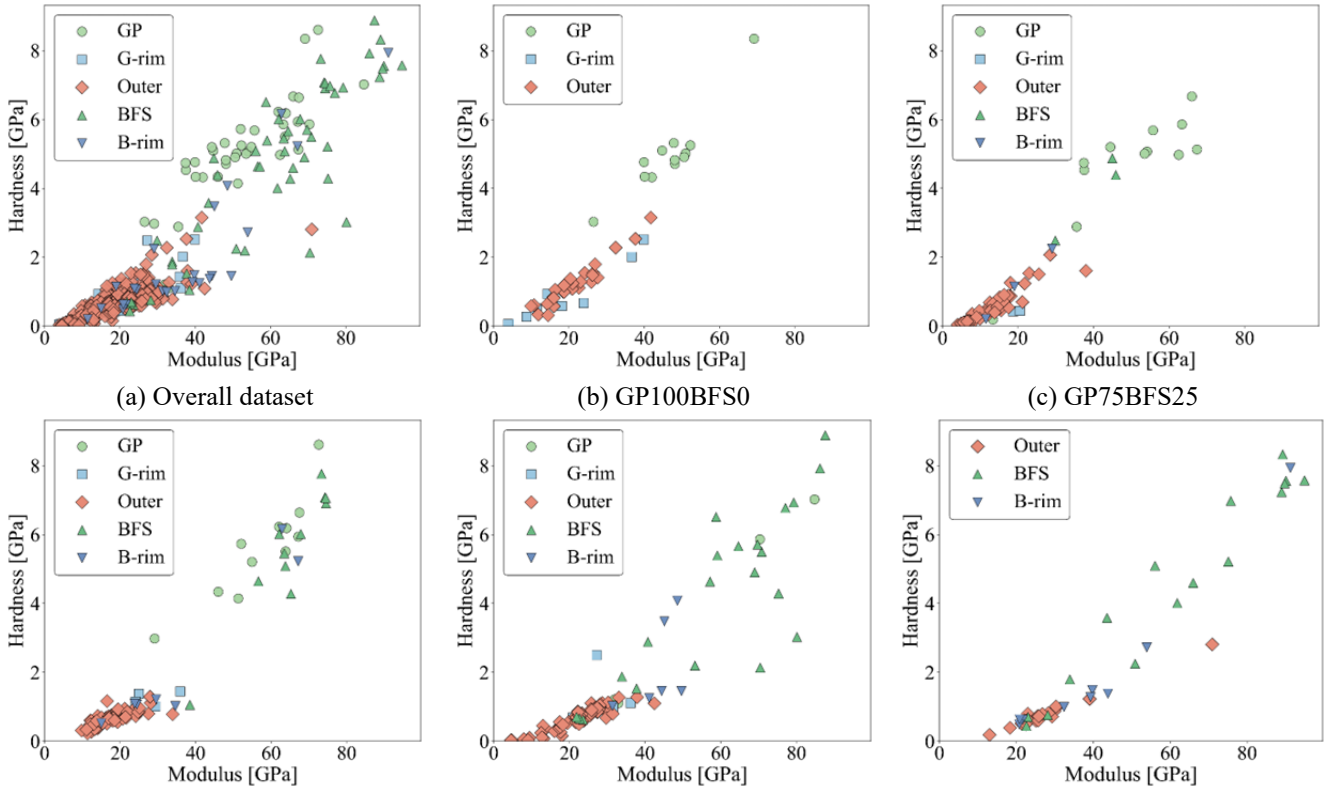

Fig. 10 Manually classified micromechanical properties analyzed from grid nanoindentation

it was placed on unreacted particles, rim regions, or the outer. Representative EDS line scanning results were used to verify typical chemical gradients across these regions and to support the phase assignments.

The nanoindentation data exhibited heteroscedastic distributions that varied according to the GP/BFS ratio, as shown in Fig. 8. As the GP content increased, the modulus–hardness trend displayed steeper slopes ranging from 0.09 to 0.13, indicating compositional changes in the reaction products. EDS mapping and line scanning indicate that GP-dominant systems tend to yield N–S–H gels (You *et al.* 2023a), whereas higher BFS contents favor the formation of C–N–A–S–H gels, which typically demonstrate a higher modulus (Fang and Zhang 2020, Lee *et al.* 2016, Nemecek *et al.* 2011, Thomas *et al.* 2018).

These chemical differences significantly influence the micromechanical response of the outer across the mixtures. In the GP100BFS0 composition, where reactive Ca and Al levels are low, the dominant reaction product is expected to be N–S–H gel. By contrast, mixtures containing BFS are likely to form C–N–A–S–H gels because of the increased availability of Ca and Al sources. Prior studies have reported that the modulus and hardness values of N–A–S–H and C–N–A–S–H gels are distributed in overlapping ranges, which makes them difficult to distinguish based on micromechanical properties alone (Arachchige *et al.* 2024, Luo *et al.* 2020a, 2020b, Thomas *et al.* 2018, Wang *et al.* 2022). Accordingly, this study adopted the practical approach used in previous studies, treating these gel-dominated regions as a single outer for classification and analysis (Arachchige *et al.* 2024).

The micromechanical properties of AAMs were assessed using nanoindentation measurements of E and H, with phase-specific values derived from manual classification of the indentation points. Five phases were identified: outer, GP particles, BFS particles, and their corresponding rims (G- and B-rim). Fig. 9 and Table 3 summarize the results.

The outer encompasses a mixture of gels across the overall datasets. It was manually classified within each mixture, enabling a comparison of average values across systems. The outer consistently displayed the lowest E across all mixtures, ranging from 13.3 to 26.9 GPa with H less than 1.2 GPa. These values reflect the relatively low density and weak cross-linking of reaction product in this phase, particularly in GP-rich mixtures. GP100BFS0 and GP75BFS25 exhibited lower E values (21.4 and 13.3 GPa, respectively), likely due to the lack of reactive Ca and Al reported in Fig. 6. GP particles demonstrated high micromechanical properties, with elastic moduli surpassing 45 GPa in all mixtures. In GP50BFS50, GP achieved the highest values (E = 57.3 GPa, H = 5.6 GPa), suggesting that the incorporation of BFS did not compromise the stiffness of the remaining unreacted glass particles.

G-rim phases exhibited significant variability based on BFS content. In the GP100BFS0 and GP75BFS25 samples, G-rims demonstrated markedly lower mechanical properties (E < 18 GPa, H < 1 GPa), accompanied by extensive microcracking visible in the BSE images (Fig. 5). These values were comparable to or even less than those of the

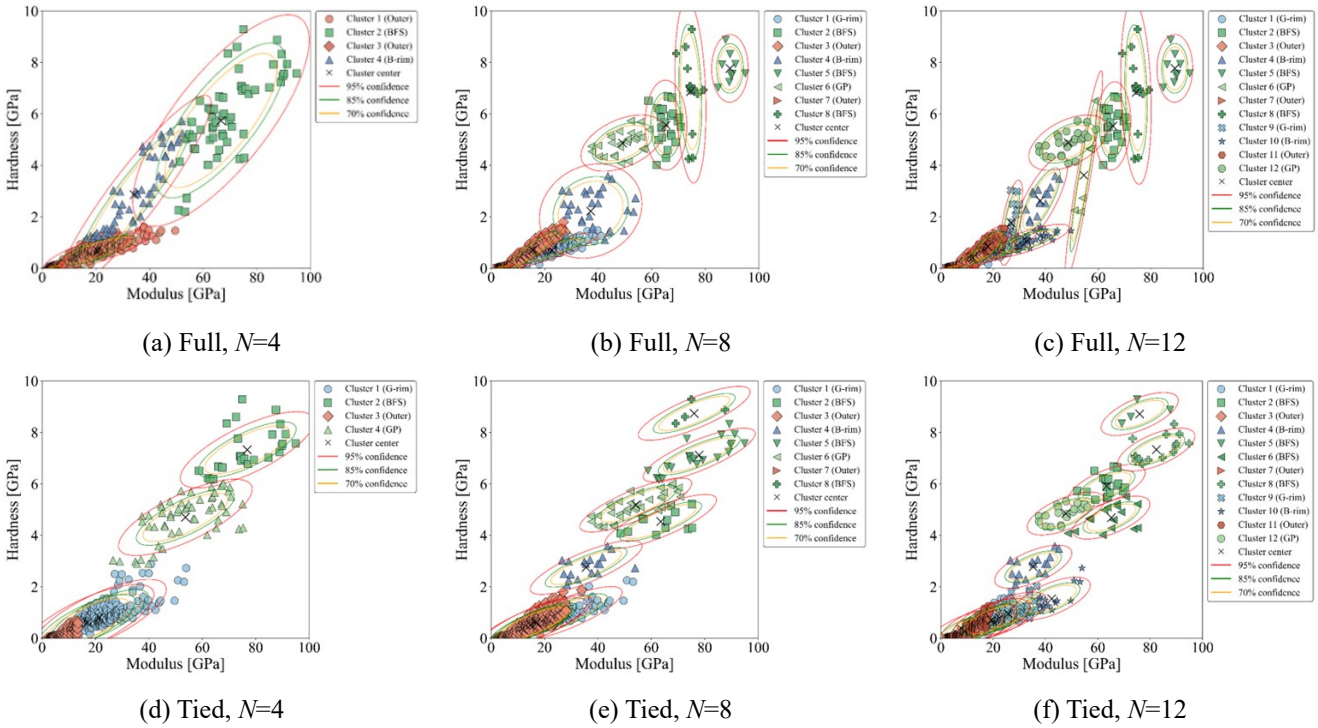

(a) Full, N=4 (b) Full, N=8 (c) Full, N=12

(d) Tied, N=4 (e) Tied, N=8 (f) Tied, N=12

Fig. 11 Gaussian mixture model clustering results in the *E*-*H* domain for different numbers of clusters (N = 4, 8, and 12), tested under both full (a)-(c) and tied (d)-(f) covariance assumptions

outer, indicating weak interfacial development. By contrast, the G-rims in GP50BFS50 and GP25BFS75 showed improved modulus ($E \approx 28$ GPa), consistent with the observed increases in Ca and Al concentrations near the interfaces (Fig. 6).

BFS particles displayed the highest E among all phases, ranging from 40.2 to 64.9 GPa. The corresponding B-rims exhibited slightly lower yet still high-modulus values (19.8–43.3 GPa), suggesting robust gel formation and effective interfacial bonding. In the GP0BFS100 mixture, B-rims maintained a high elastic modulus of 40.4 GPa, whereas the outer displayed a relatively high average modulus of 26.9 GPa, reflecting the dominant influence of BFS on structure of reaction products. The observed variability in B-rim stiffness values may partly stem from the inherently heterogeneous nature of AAMs as well as the highly localized nature of nanoindentation measurements. In particular, micro-defects near the rim region, as observed in Fig. 5c, could contribute to this variation in certain mixtures such as GP50BFS50.

The micromechanical response of each phase is determined by variations in the availability of reactive species, particularly Ca and Al, which are influenced by the precursor composition. In GP-only materials, rims were poorly developed as illustrated in Fig. 5, resulting in low E due to limited Ca and Al concentrations (Fig. 7). By contrast, increasing BFS content enhanced E of both rims and the outer. These findings align with the chemical composition profiles presented in Fig. 6. The manually classified indentation data provides a reference for evaluating the accuracy of the GMM predictions.

3.2 Unsupervised phase classification using Gaussian mixture model

3.2.1 Clustering results

To classify the material phases, GMM clustering was applied to the overall nanoindentation dataset. Based on the BIC results displayed in Fig. 10, three representative numbers of clusters (N = 4, 8, and 12) were selected. The values N = 4 and N = 8 correspond to local minimum in the BIC curve. N = 12 was included to explore phase resolution under a relatively high number of clusters with acceptable model complexity.

Fig. 11 shows the results of unsupervised micromechanical phase classification using GMM. Clustering was performed on the nanoindentation dataset in the *E*–*H* domain. Three different numbers of clusters (N = 4, 8, and 12) were tested under two covariance assumptions: full (a)-(c) and tied (d)-(f). Each cluster was modeled as a multivariate normal distribution, with the statistical spread for each represented by ellipses corresponding to 95%, 85%, and 70% confidence levels (red, green, and yellow, respectively). The color of each cluster was assigned according to the location of its centroid, which was matched to the closest reference phase identified in the experimental classification (particle, rim, or outer).

In the full covariance case, increasing N generally led to greater overlap between neighboring clusters, reducing the clarity of their boundaries. When N = 4, which is fewer than the five expected micromechanical phases, the model was unable to reproduce the phase separation accurately, resulting in several phases being grouped together. As N increased, some clusters began to span both rim and outer

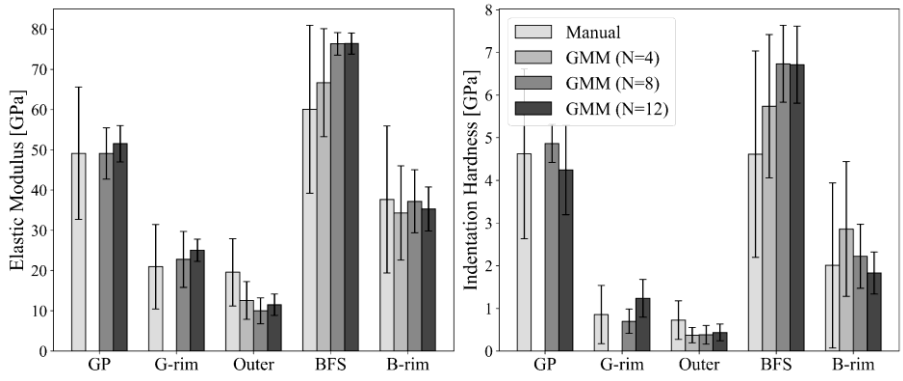

(a) Full

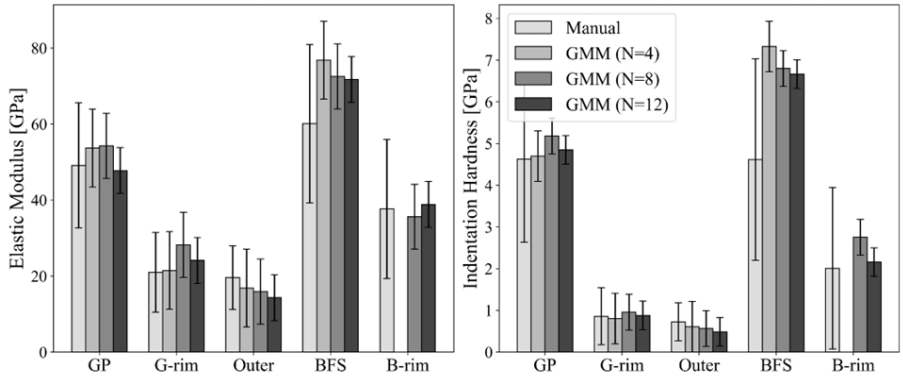

(b) Tied

Fig. 12 Comparison of average elastic modulus (left) and hardness (right) by phase between manual labeling and GMM results at N = 4, 8, and 12. Missing bars indicate undetected phases

regions. This trend indicates potential overfitting due to the increased number of free parameters. Similarly, prior studies reported that using only a few clusters in GMM fails to reliably distinguish the micromechanical properties of N–A–S–H gel due to inadequate resolution of phase heterogeneity (Luo *et al.* 2021, 2020a, 2020b). Consequently, some of the resulting clusters may reflect local variations or outliers rather than physically meaningful phases. The emergence of multiple small clusters with irregular shapes further suggests reduced robustness in classification. Therefore, the full covariance model is less suitable for reliably identifying distinct phases, particularly with a high number of clusters.

By contrast, the tied covariance model produced more consistent cluster shapes and clearer boundaries. In this model, all clusters share a common covariance matrix. At N = 8 and N = 12, the clusters remained well separated and closely aligned with the reference phase classification (Fig. 9).

This stability suggests the tied model more effectively captures the intrinsic structure of the data. In addition, the cluster centroids followed the expected micromechanical trend, transitioning from high-modulus particles to low modulus outer region. Furthermore, even at N = 12, the tied model did not produce redundant or overlapping clusters. These results indicate that the tied model can better distinguish mechanically distinct phases while maintaining clear separation.

3.3 Comparison between GMM and manual phase classification

To evaluate the effectiveness of unsupervised GMM clustering, we compared the predicted phases with manual classifications in two aspects: (1) average elastic modulus and hardness (Fig. 12) and (2) estimated volume fractions (Fig. 13) using the evaluation metrics summarized in Table 4 and introduced in Eqs. (4)-(6).

In the full covariance model, N = 4 could not distinguish the rim phases, instead grouping them with adjacent phases. Because the alkali-activated GP-BFS system is considered to consist of five distinct phases, N = 4 is insufficient to represent all of them. This leads to significant deviations from manual classification, with a centroid error of D_4 = 0.51. At N = 8, the centroid deviation slightly increased to D_8 = 0.54. The B-rim phase showed a modulus of 35.3 GPa, exceeding the upper bound of the manual range (up to 27.6 GPa) and indicating overestimation. The outer modulus was 11.5 GPa, which was lower than the reference range of 13.3–26.9 GPa. At N = 12, the centroid deviation remained the same (D_{12} = 0.54), and similar trends persisted. Although the model did not exhibit inflated standard deviations, it struggled to define clear boundaries between overlapping phases. These results imply that the flexibility of the full covariance model leads to unstable centroid locations when the feature distributions of different phases were close to each other.

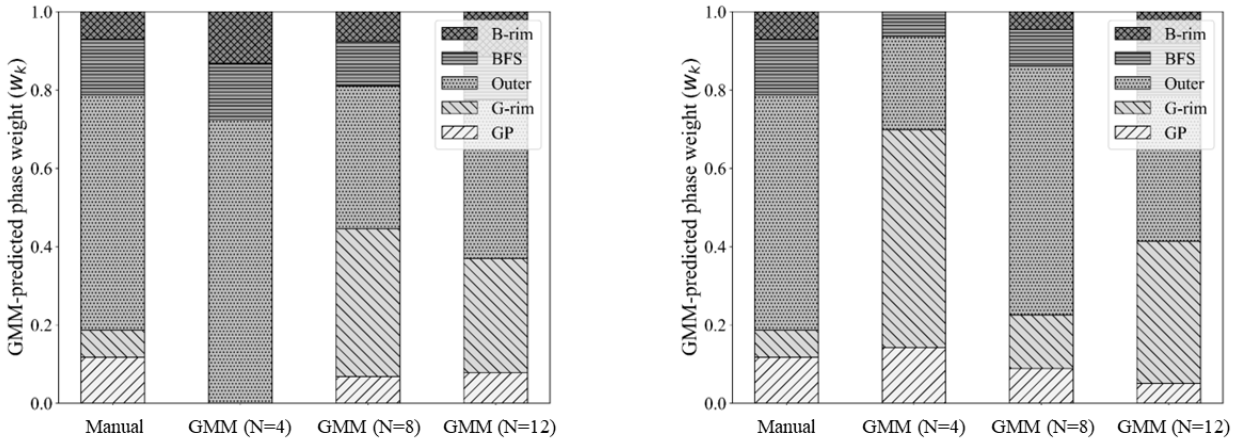

(a) Full (b) Tied

Fig. 13 Phase fraction comparison between manual and GMM results (N = 4, 8, 12)

Table 4 Evaluation of GMM clustering results for each N

Covariance	N	D_N	δ_N
Full	4	0.51	0.07
	8	0.54	0.13
	12	0.54	0.11
Tied	4	0.46	0.20
	8	0.56	0.04
	12	0.48	0.12

*D_N: Average centroid error; δ_N: total difference in phase fractions

As N increased, the tied covariance model showed consistent centroid values for the outer and G-rim phases.

At N = 8, the outer exhibited an elastic modulus of 16.9 GPa and hardness of 0.61 GPa. These values are within the manual reference ranges of 13.3–26.9 GPa and 0.6–1.2 GPa. The G-rim centroid exhibited a modulus of 28.2 GPa and hardness of 0.95 GPa, which was slightly higher than the upper bound of the manual modulus range (up to 28.2 GPa) but within acceptable variation. The centroid deviation at this point was D_8 = 0.56. At N = 12, the G-rim centroid shifted to 22.4 GPa in modulus and 0.80 GPa in hardness, both clearly within the manual ranges. The outer showed values of 14.5 GPa and 0.50 GPa, indicating slight underestimation in hardness. The overall centroid deviation decreased to D_{12} = 0.48. These results suggest that the tied model effectively reduces centroid drift and avoids distortion in overlapping regions. The use of a shared covariance matrix aids in maintaining consistent cluster boundaries and improves agreement with physically observed phases. To further assess clustering performance, the predicted phase fractions presented in Fig. 13 and the evaluation metrics in Table 4 were analyzed. These metrics facilitate a quantitative evaluation of how effectively the GMM models replicate the manually classified phase composition.

In the full covariance model, all tested N values exhibited notable discrepancies from the manual reference. At N = 4, rim phases were in distinguishable and instead were absorbed into adjacent clusters, particularly BFS and outers. This resulted in a significant phase fraction error of δ_4 = 0.13. An increase to N = 8 did not resolve this issue; the model overestimated B-rim and underestimated outer, with δ_8 = 0.12. Even at N = 12, although δ_{12} slightly decreased to 0.09, the phase boundaries remained unstable, and the predicted compositions deviated significantly from the manual reference. These limitations derive from the flexibility of the full model, where unconstrained covariance structures enable arbitrary elongation or compression of clusters. The result is often overfitting to local data distributions and the merging of physically distinct phases, particularly when their feature spaces overlap.

By contrast, the tied covariance model demonstrated improved robustness. At N = 4, it achieved a lower phase error (δ_4 = 0.08) by maintaining more distinct boundaries. As N increased to 8, the phase fractions closely matched the manual classification, where all three primary regions, that is, particle, rim (G- and B-rim), and outer, were within 5% of the reference. The overall error was minimized to δ_8 = 0.04. Even at N = 12, the model avoided over-segmentation, maintaining physically meaningful clusters and a low error of δ_{12} = 0.06. The statistical constraint of shared covariance in the tied model regularized the cluster shapes, suppressing noisy or distorted segmentation and promoting better alignment with heterogeneous phases of AAMs. Of the configurations tested, the tied model at N = 8 provided the most consistent agreement with the reference, in terms of both phase composition and cluster separation quality.

Phase assemblage is influenced by the chemical composition of the precursor and the alkaline activator. An increase in water content does not provide additional Si, Al, or Ca, and thus does not alter the phase chemistry (Provis *et al.* 2015, Tu and Zhang 2024). However, experimental studies on AAMs have shown that a higher water to binder ratio increases both total porosity and the proportion of capillary pores (Chen *et al.* 2022, Duan *et al.* 2015, Kong *et al.* 2007). The effects of these microstructural changes on micromechanical properties are beyond the scope of this study and will be addressed in future research.

4. Conclusions

This study proposed a reproducible framework for unsupervised phase classification in alkali-activated glass powder–blast furnace slag (GP–BFS) systems using nanoindentation and Gaussian mixture models (GMMs). The main conclusions are as follows:

• Five distinct phases, GP, BFS, G-rim, B-rim, and outer, were identified through microstructural and chemical correlation, serving as references for model evaluation.

• The optimal number of clusters for the GMM was determined using the Bayesian Information Criterion (BIC). Among the tested values, N = 8 was selected based on its ability to balance model simplicity and clustering accuracy.

• The full covariance model exhibited overfitting tendencies as the number of clusters increased, resulting in unstable phase boundaries and misclassification of rim or low-modulus regions. In contrast, the tied covariance model with N = 8 achieved stable and interpretable clustering, successfully distinguishing key phases while maintaining realistic phase boundaries and proportions.

• Quantitative comparison with manual classification confirmed that the tied covariance model with N = 8 most accurately reproduced both micromechanical properties and phase proportions. This demonstrates its potential as a reliable, automated alternative to time-consuming and subjective manual classification. The proposed approach enables efficient and reproducible analysis of micromechanical heterogeneity in GP–BFS systems, facilitating better understanding of microstructure–property relationships for material optimization.

• Further research is needed to investigate how variations in the water-to-precursor (W/P) ratio affect the separability and micromechanical properties of individual phases. In addition, classification of the outer could be further improved by incorporating local Ca/Si and Al/Si ratios as chemical features in the clustering process. This enhancement would enable identification between weakly-reacted products and the pore-filling matrix.

Appendix A. Parameter identification by grid nanoindentation

From the load–depth response shown in Fig. A.1, two micromechanical parameters, namely indentation hardness (H) and elastic modulus (E)—were calculated following the Oliver–Pharr method (Oliver *et al.* 1992). These parameters quantify local resistance to plastic and elastic deformation, respectively. The indentation hardness H is given by

$$H = \frac{P_{\max}}{A} \tag{7}$$

where $P_{\max}$ is the maximum applied load, and A is the projected contact area, respectively. The contact area A is given by

$$A = C_0 h_c^2 \tag{8}$$

where C_0 = 24.5 is the geometric constant for a Berkovich indenter, and h_c is the contact depth, respectively. The contact depth h_c is given by

$$h_c = h_{\max} - \varepsilon \frac{P}{S} \tag{9}$$

where $h_{\max}$ is the maximum indentation depth, P is the instantaneous load, S is the unloading stiffness, and ε = 0.75 is a geometric correction constant, respectively (Oliver *et al.* 1992). The reduced modulus E_r is given by

$$\frac{1}{E_r} = \frac{(1-\nu^2)}{E} + \frac{(1-\nu_i^2)}{E_i} \tag{10}$$

where E and ν are the Young's modulus and Poisson's ratio of the specimen, and E_i = 1,140 GPa and ν_i = 0.07 are those of the diamond indenter, respectively (Oliver *et al.* 1992). A Poisson's ratio of ν = 0.20 was used, following (Luo *et al.* 2020a). Alternatively, E_r is given by

$$E_r = \frac{S\sqrt{\pi}}{2\sqrt{A}} \tag{11}$$

where S is the unloading stiffness, and A is the projected contact area, respectively. The stiffness S is given by

$$S = \left.\frac{dP}{dh}\right|_{h=h_{\max}} \tag{12}$$

where P is the applied load, and h is the indentation depth, respectively. This framework provides a consistent basis for extracting micromechanical properties from indentation data, allowing phase-level comparison in multiphase alkali-activated matrices (Arachchige *et al*. 2024, Bondar *et al.* 2011, Hu and Li 2014, Luo *et al*. 2020a, Thomas and Peethamparan 2015).

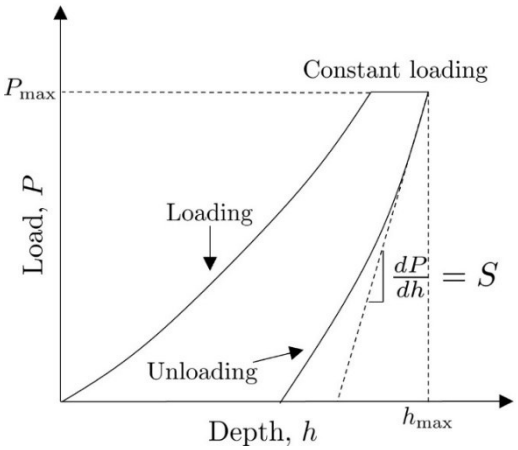

Fig. A.1 load-depth curve of nanoindentation

Acknowledgments

This research was financially supported by the National Research Foundation of Korea (NRF) grant funded by the Korea government (MSIT) (No. RS-2021-NR060085).

References

Adesina, A. and Das, S. (2020), "Influence of glass powder on the durability properties of engineered cementitious composites", *Constr. Build. Mater.*, **242**, 118199

Ali, H.A., Sun, K., Xuan, D., Lu, J.X., Cyr, M. and Poon, C.S. (2023), "Recycling of high-volume waste glass powder in alkali-activated materials: An efflorescence mitigation strategy", *J. Build. Eng.*, **65**, 105756

Arachchige, R.M., Olek, J., Rajabipour, F. and Peethamparan, S. (2024), "Phase identification and micromechanical properties of non-traditional and natural pozzolan based alkali-activated materials", *Constr. Build. Mater.*, **441**, 137478

Bishop, C.M., Nasrabadi, N.M. (2006), "Pattern recognition and machine learning", *Springer*, **4**

Bondar, D., Lynsdale, C.J., Milestone, N.B., Hassani, N. and Ramezanianpour, A.A. (2011), "Engineering properties of alkali-activated natural pozzolan concrete", *ACI Mater. J.*, **108**, 64-72

Canakci, H., Aram, A. and Celik, F. (2016), "Stabilization of clay with waste soda lime glass powder", *Procedia Eng.*, **161**, 600-605.

Cercel, J., Adesina, A. and Das, S. (2021), "Performance of eco-friendly mortars made with alkali-activated slag and glass powder as a binder", *Constr. Build. Mater.*, **270**, 121457.

Chen, S., Ruan, S., Zeng, Q., Liu, Y., Zhang, M., Tian, Y. and Yan, D. (2022), "Pore structure of geopolymer materials and its correlations to engineering properties: A review", *Constr. Build. Mater.*, **328**, 127064.

Chen, X., Hou, D., Han, Y., Ding, X. and Hua, P. (2021), "Clustering analysis of grid nanoindentation data for cementitious materials", *J. Mater. Sci.*, **56**, 12238-12255.

Du, H. and Tan, K.H. (2017), "Properties of high volume glass powder concrete", *Cem. Concr. Compos.*, **75**, 22-29.

Duan, P., Yan, C., Zhou, W., Luo, W. and Shen, C. (2015), "An investigation of the microstructure and durability of a fluidized bed fly ash–metakaolin geopolymer after heat and acid exposure", *Mater. Des.*, **74**, 125-137.

Fang, G. and Zhang, M. (2020), "Multiscale micromechanical analysis of alkali-activated fly ash-slag paste", *Cem. Concr. Res.*, **135**, 106141.

Ferdous, W., Manalo, A., Siddique, R., Mendis, P., Zhuge, Y., Wong, H.S., Lokuge, W., Aravinthan, T. and Schubel, P. (2021), "Recycling of landfill wastes (tyres, plastics and glass) in construction–a review on global waste generation, performance, application and future opportunities", *Resour. Conserv. Recycl.*, **173**, 105745.

Jia, Z., Chen, C., Zhou, H. and Zhang, Y. (2020), "The characteristics and formation mechanism of the dark rim in alkali-activated slag", *Cem. Concr. Compos.*, **112**, 103682.

Kalakada, Z., Doh, J. and Zi, G. (2020), "Utilisation of coarse glass powder as pozzolanic cement—a mix design investigation", *Constr. Build. Mater.*, **240**, 117916.

Kong, D.L., Sanjayan, J.G. and Sagoe-Crentsil, K. (2007), "Comparative performance of geopolymers made with metakaolin and fly ash after exposure to elevated temperatures", *Cem. Concr. Res.*, **37**, 1583-1589.

Königsberger, M., Zelaya-Lainez, L., Lahayne, O., Pichler, B.L. and Hellmich, C. (2022), "Nanoindentation-probed Oliver–Pharr half-spaces in alkali-activated slag–fly ash pastes: Multimethod identification of microelasticity and hardness", *Mech. Adv. Mater. Struct.*, **29**, 4878-4889.

Lee, H., Vimonsatit, V. and Chindaprasirt, P. (2016), "Mechanical and micromechanical properties of alkali activated fly-ash cement based on nanoindentation", *Constr. Build. Mater.*, **107**, 95-102.

Lee, Y., Seo, S., You, I., Yun, T.S. and Zi, G. (2023), "Prediction of calcium leaching resistance of fly ash blended cement composites using artificial neural network", *Comput. Concr.*, **31**, 315-325.

Lu, J.X. and Poon, C.S. (2018), "Use of waste glass in alkali activated cement mortar", *Constr. Build. Mater.*, **160**, 399-407.

Lu, J.X., Zhan, B.J., Duan, Z.H. and Poon, C.S. (2017), "Using glass powder to improve the durability of architectural mortar prepared with glass aggregates", *Mater. Des.*, **135**, 102-111.

Luo, Z., Li, W., Gan, Y., He, X., Castel, A. and Sheng, D. (2021), "Nanoindentation on micromechanical properties and microstructure of geopolymer with nano-SiO_2 and nano-TiO_2", *Cem. Concr. Compos.*, **117**, 103883.

Luo, Z., Li, W., Gan, Y., Mendu, K. and Shah, S.P., (2020a), "Applying grid nanoindentation and maximum likelihood estimation for N–A–S–H gel in geopolymer paste: Investigation and discussion", *Cem. Concr. Res.*, **135**, 106112

Luo, Z., Li, W., Gan, Y., Mendu, K. and Shah, S.P., (2020b), "Maximum likelihood estimation for nanoindentation on sodium aluminosilicate hydrate gel of geopolymer under different silica modulus and curing conditions", *Compos. B Eng.*, **198**, 108185

Maraghechi, H., Salwocki, S. and Rajabipour, F. (2017), "Utilisation of alkali activated glass powder in binary mixtures with portland cement, slag, fly ash and hydrated lime", *Mater. Struct*., **50**, 1-14.

Mirzahosseini, M. and Riding, K.A. (2015), "Influence of different particle sizes on reactivity of finely ground glass as supplementary cementitious material (SCM)", *Cem. Concr. Compos.*, **56**, 95-105.

Mota Gassó, B. (2015), "Impact of alkali salts on the kinetics and microstructural development of cementitious systems", *Tech. Rep.*, EPFL.

Nemecek, J., Smilauer, V. and Kopecky, L. (2011), "Nanoindentation characteristics of alkali-activated aluminosilicate materials", *Cem. Concr. Compos.*, **33**, 163-170.

Oliver, W.C. and Pharr, G.M. (1992), "An improved technique for determining hardness and elastic modulus using load and displacement sensing indentation experiments", *J. Mater. Res.*, **7**, 1564-1583.

Provis, J.L., Palomo, A. and Shi, C. (2015), "Advances in understanding alkali-activated materials", *Cem. Concr. Res.*, **78**, 110-125.

Rajabipour, F., Giannini, E., Dunant, C., Ideker, J.H. and Thomas, M.D. (2015), "Alkali–silica reaction: Current understanding of the reaction mechanisms and the knowledge gaps", *Cem. Concr. Res.*, **76**, 130-146.

Saccani, A. and Bignozzi, M.C. (2010), "ASR expansion behavior of recycled glass fine aggregates in concrete", *Cem. Concr. Res.*, **40**, 531-536.

Samarakoon, M., Ranjith, P. and De Silva, V. (2020), "Effect of soda-lime glass powder on alkali-activated binders: Rheology, strength and microstructure characterization", *Constr. Build. Mater.*, **241**, 118013.

Schwarz, G. (1978), "Estimating the dimension of a model", *Ann. Stat.*, **6**, 461-464.

Shayan, A. and Xu, A. (2006), "Performance of glass powder as a pozzolanic material in concrete: A field trial on concrete slabs", *Cem. Concr. Res.*, **36**, 457-468.

Shi, C. and Zheng, K. (2007), "A review on the use of waste

glasses in the production of cement and concrete", *Resour. Conserv. Recycl.*, **52**, 234-247.
Shi, C., Wu, Y., Riefler, C. and Wang, H. (2005), "Characteristics and pozzolanic reactivity of glass powders", *Cem. Concr. Res.*, **35**, 987-993.
Singh, B., Ishwarya, G., Gupta, M. and Bhattacharyya, S. (2015), "Geopolymer concrete: A review of some recent developments", *Constr. Build. Mater.*, **85**, 78–90.
Sun, L., Kim, M., Doh, J.H. and Zi, G. (2021a), "A novel method of crushing glass aggregates to reduce the alkali-silica reaction", *KSCE J. Civ. Eng.*, **25**, 4763-4770.
Sun, R., Fang, C., Zhang, H., Ling, Y., Feng, J., Qi, H. and Ge, Z. (2021b), "Chemomechanical properties of alkali-activated slag/fly ash paste incorporating white mud", *Constr. Build. Mater.*, **291**, 123312.
Thomas, R., Gebregziabiher, B.S., Giffin, A. and Peethamparan, S. (2018), "Micromechanical properties of alkali-activated slag cement binders", *Cem. Concr. Compos.*, **90**, 241-256.
Thomas, R.J. and Peethamparan, S. (2015), "Alkali-activated concrete: Engineering properties and stress–strain behavior", *Constr. Build. Mater.*, **93**, 49-56.
Tu, W. and Zhang, M. (2024), "Multiscale microstructure and micromechanical properties of alkali-activated concrete: A critical review", *Cem. Concr. Compos.*, 105664.
Wang, J., Hu, Z., Chen, Y., Huang, J., Ma, Y., Zhu, W. and Liu, J. (2022), "Effect of Ca/Si and Al/Si on micromechanical properties of C(-A)-S-H", *Cem. Concr. Res.*, **157**, 106811.
Wilson, W., Rivera-Torres, J., Sorelli, L., Durán-Herrera, A. and Tagnit-Hamou, A. (2017), "The micromechanical signature of high-volume natural pozzolan concrete by combined statistical nanoindentation and SEM-EDS analyses", *Cem. Concr. Res.*, **91**, 1-12.
Wilson, W., Soliman, N.A., Sorelli, L. and Tagnit-Hamou, A. (2019), "Microchemo-mechanical features of ultra-high performance glass concrete (UHPGC)", *Theor. Appl. Fract. Mech.*, **104**, 102373.
Xiao, R., Zhang, Y., Jiang, X., Polaczyk, P., Ma, Y. and Huang, B. (2021), "Alkali-activated slag supplemented with waste glass powder: Laboratory characterization, thermodynamic modelling and sustainability analysis", *J. Clean. Prod.*, **286**, 125554.
Yoo, D.Y., Lee, S.K., You, I., Oh, T., Lee, Y. and Zi, G. (2022a), "Development of strain-hardening geopolymer mortar based on liquid-crystal display (LCD) glass and blast furnace slag", *Constr. Build. Mater.*, **331**, 127334.
Yoo, D.Y., Lee, Y., You, I., Banthia, N. and Zi, G. (2022b), "Utilization of liquid crystal display (LCD) glass waste in concrete: A review", *Cem. Concr. Compos.*, **130**, 104542.
You, I., Lee, Y., Yoo, D.Y. and Zi, G. (2022), "Influence of liquid crystal display glass powder on the tensile performance of ultra-high-performance fiber-reinforced concrete", *J. Build. Eng.*, **57**, 104901.
You, I., Seo, S., Kim, M., Lee, S.J., Lee, N., Lee, Y. and Yoo, D.Y. (2023a), "ASR potential of alkali-activated soda-lime glass powder in the absence of calcium sources", *Cem. Concr. Compos.*, **139**, 105027.
You, I., Yoo, D.Y., Doh, J.H. and Zi, G. (2021), "Performance of glass-blended cement produced by intergrinding and separate grinding methods", *Cem. Concr. Compos.*, **118**, 103937.
You, I., Yoo, D.Y., Lee, S.J., Lee, Y. and Zi, G. (2023b), "A combination of liquid–crystal display glass powder and slag in alkali-activated material", *Constr. Build. Mater.*, **369**, 130527.
Zhang, B., He, P. and Poon, C.S. (2020), "Optimizing the use of recycled glass materials in alkali activated cement (AAC) based mortars", *J. Clean. Prod.*, **255**, 120228.
Zhang, L. and Zhai, J. (2021), "Application of response surface methodology to optimize alkali-activated slag mortar with limestone powder and glass powder", *Struct. Concr.*, **22**, e430-e441.